Wall-modeled large eddy simulation of turbulent heat transfer by the lattice Boltzmann method

Wall-modeled large eddy simulation of turbulent heat transfer by the lattice Boltzmann method

Y. Kuwata*, K. Suga

Department of Mechanical Engineering, Osaka Prefecture University, Sakai, Osaka 599–8531, Japan

Abstract

A novel implementation route of the wall-function method to the lattice Boltzmann method (LBM) is proposed to extend the applicability of the LBM for high Reynolds number turbulent heat transfer in complex geometries. The proposed immersed virtual wall method assumes the virtual wall layer beneath the wall which satisfies the slip wall conditions allowing the subsurface heat and fluid flows within the solid wall. For the validation tests, the D3Q27 multiple-relaxation-time LBM and D3Q19 regularized LBM are used to simulate flow and scaler fields, respectively, and the standard log-law based wall-function method is used. Validation tests against turbulent flows in a two-dimensional channel, circular pipe, channel with two-dimensional constraints confirms that the developed method can deal with complex curvilinear walls and yield grid independent solution with satisfactory accuracy. In addition, the developed method can be applied from partially to highly underresolved conditions, and has a great potential in predicting high Prandtl number flows.

Keywords: Lattice Boltzmann method, Wall function, Large eddy simulation, Turbulent heat transfer

*Corresponding author
Email address: kuwata@me.osakafu-u.ac.jp (K. Suga)

1. Introduction

The lattice Boltzmann method (LBM) has been accepted as an extremely suitable tool for eddy resolving simulations of a turbulent flow in complicated geometries. Unlike the conventional computational fluid dynamic (CFD) solver that deals with the discretized Navier-Stokes equations, the LBM solves the time evolution of the particle distribution function based on the discretized gas kinetic equations. The resulting formulation of the LBM offers many advantages over the conventional CFD solver as regards the computational efficiency and accuracy [1, 2, 3, 4, 5]. The most notable feature of the LBM is the considerable simplicity of the algorithm which proceeds by repetition of the collision and streaming steps. In the collision step the particle distribution function is locally relaxed toward the equilibrium state while the post-collision particle distribution function moves to the neighboring lattice nodes in the streaming step. This distinct separation of the local and non-local computations enhances the efficiency of parallel computation. In addition, the efficiency of the LBM is further enhanced due to a release from internal iteration for solving the Poisson's equation. Moreover, another important feature of the LBM is employing a regular grid with equal spacing in which non-body-fitted meshes are used to describe the flow around complex geometries. This feature significantly saves the computational effort related to a mesh generation and reduces numerical errors arising from a coordinate transformation procedure.

Despite the above mentioned advantages of the LBM, several deficits of the LBM, namely the truncation errors and numerical stability issues, make it difficult to applies the LBM to turbulent flow simulations. However, these deficits have been successfully recovered by the use of improved collision models (e.g., multiple-relaxation-model [6, 7], central moment model [8, 9], and cumulant model [10]) and an increased discrete velocity components [11, 12, 13, 14, 15]. A large number of rigorous validation studies of the LBM based direct numerical simulation (DNS) in fundamental turbulent flows such as wall-bounded turbulence [11, 7, 16, 17] and homogeneous decaying turbulence [18, 19, 20, 21] was performed, and those studies have established that the LBM is an alternative DNS scheme for simulating flows in complex geometries. Also, the author groups made an effort to improve the LBM [15, 22], and we have performed LBM of turbulence in complex geometries [22, 23, 24, 25, 26, 27] most of which are difficult to dealt with the conventional Navier-Stokes solver. In addition to the applications of the LBM in fundamental research based on the DNS, the LBM is used as the engineering large eddy simulation (LES) tool in which large-scale turbulent motions are directly resolved by the grid while the effects of the unresolved sub-grid-scale (SGS) turbulence are modeled by the SGS turbulence model. The application examples of the LBM-LES are a porous medium flow [28, 29], an urban canopy flow [4, 30], an internal combustion engine flows [16], an indoor airflow [31], and a turbulent jet flow [32, 33]. However, even though the SGS turbulence model is adopted to reduce the computational cost, the grid resolution should be fine enough to resolve the most energetic and dynamic turbulence motions in an inner layer, and the inner-layer of a wall-bounded turbulent flow becomes progressively thinner as the Reynolds number increases. Therefore, the computational resource to correctly resolve turbulence in the inner-layer becomes prohibitive for higher Reynolds number flows.

One solution to overcome this problem is to simply replace the inner-layer region with a turbulence model. In other words, the wall shear stress is directly given by the modeled thin-layer approximate equations without resolving near wall turbulent motions. This strategy is referred to as a wall-function method and originally developed for Reynolds Average Navier-Stokes (RANS) simulations by [34] who assumed the law of the wall to prescribe the wall shear stress. As for the conventional Navier-Stokes solvers, the wall-modeled LES based on the wall-function have achieved considerable successes in predicting higher Reynolds number turbulent flows [35, 36, 37, 38], which is still incapable of the wall-resolved LES even with the modern super computer. However, in comparison to the Navier-Stokes solvers, there is much less progress in the development of the wall-modeled LBM-LES. The pioneering work on the wall-modeled LBM-LES was conducted by [39] who reconstructed the particle distribution function at the first grid point off the wall based on the quasi-analytical models that gave the velocity profile inside the boundary layer. The developed model was successfully validated through the turbulent channel flow in severely under-resolved situations. The other implementation approach was proposed by [40]. They imposed an appropriate slip velocity at the boundary surface to satisfy the skin friction requirement. The validation test in the turbulent channel flows suggested that the developed method had a potential to predict turbulence in severely under-resolved situations although the agreement of the Reynolds stress and mean velocity with the DNS results was not perfect.

The implementation approaches proposed by [39, 40] showed successes in predicting the turbulent channel flows. However, as far as the authors know, there is no wall-modeled LBM-LES method that is validated against complicated geometries including curvilinear walls. The aim of this study is to develop a new implementation approach of the wall-function to the LBM that can predict turbulent heat transfer in complicated geometries with satisfying accuracy. The required abilities of the new method under consideration are less grid dependency on the solution and high applicability for complicated geometries without deteriorating mass and momentum conservation laws. Although there are many wall-function models and LBM models, the goal of this study is to develop an implementation method for the wall-function. Hence, we use the standard wall-function method that relies on the conventional law of the wall, and the LBM models of [7, 28] are used for simulating time-dependent turbulent heat transfer, and applications of more elaborate wall-function models or other LBM models will be the focus of our future work.

2. Lattice Boltzmann method

The lattice Boltzmann method has many advantages such as the simplicity of the wall treatment, high spatial locality of the calculations, high accuracy coming from the nature of its low numerical dissipation and dispersion. These great advantages motivate us to employ the LBM to deal with fundamental turbulent flow problems in a complicated geometry. In the case of the LBM, there are several possible choices for the discrete velocity and collision models for three-dimensional simulations. This study chooses the D3Q27 multiple-relaxation-time lattice Boltzmann method (MRT-LBM), which was developed by our group and rigorously validated by conducting DNSs of a turbulent channel flow, pipe flow, duct flow, and porous medium flows [7].

The time evolution of the particle distribution function f_α of the MRT-LBM can be written as

$$\begin{aligned} \mid f(\boldsymbol{x}+\boldsymbol{e}_\alpha \delta t, t+\delta t)\rangle - \mid f(\boldsymbol{x},t)\rangle \;&=\; -\boldsymbol{M^{-1}}\hat{\boldsymbol{S}}\left[\mid m(\boldsymbol{x},t)\rangle - \mid m^{eq}(\boldsymbol{x},t)\rangle\right] \\ &\quad +\boldsymbol{M^{-1}}\left(\boldsymbol{I}-\frac{\hat{\boldsymbol{S}}}{\boldsymbol{2}}\right)\boldsymbol{M} \mid F(\boldsymbol{x},t)\rangle \delta t, \end{aligned} \tag{1}$$

where $|f\rangle$ is $|f\rangle = (f_0, f_1, \cdots, f_{26})^T$, δt is the time step. The discrete velocity vector components are

$$[\boldsymbol{e}_0\ \boldsymbol{e}_1\ \boldsymbol{e}_2\ \boldsymbol{e}_3\ \boldsymbol{e}_4\ \boldsymbol{e}_5\ \boldsymbol{e}_6\ \boldsymbol{e}_7\ \boldsymbol{e}_8\ \boldsymbol{e}_9\ \boldsymbol{e}_{10}\ \boldsymbol{e}_{11}\ \boldsymbol{e}_{12}\ \boldsymbol{e}_{13}\ \boldsymbol{e}_{14}\ \boldsymbol{e}_{15}\ \boldsymbol{e}_{16}\ \boldsymbol{e}_{17}\ \boldsymbol{e}_{18}\ \boldsymbol{e}_{19}\ \boldsymbol{e}_{20}\ \boldsymbol{e}_{21}\ \boldsymbol{e}_{22}\ \boldsymbol{e}_{23}\ \boldsymbol{e}_{24}\ \boldsymbol{e}_{25}\ \boldsymbol{e}_{26}]/c$$
$$= \begin{bmatrix} 0 & 1 & 0 & -1 & 0 & 0 & 0 & 1 & -1 & -1 & 1 & 1 & 0 & -1 & 0 & 1 & 0 & -1 & 0 & 1 & -1 & -1 & 1 & 1 & -1 & -1 & 1 \\ 0 & 0 & 1 & 0 & -1 & 0 & 0 & 1 & 1 & -1 & -1 & 0 & 1 & 0 & -1 & 0 & 1 & 0 & -1 & 1 & 1 & -1 & -1 & 1 & 1 & -1 & -1 \\ 0 & 0 & 0 & 0 & 0 & 1 & -1 & 0 & 0 & 0 & 0 & 1 & 1 & 1 & 1 & -1 & -1 & -1 & -1 & 1 & 1 & 1 & 1 & -1 & -1 & -1 & -1 \end{bmatrix},$$

where $c = \Delta/\delta t$ with Δ is the lattice spacing. The identity matrix $\boldsymbol{I}$ and transforming matrix $\boldsymbol{M}$ are a 27×27 matrix. The transforming matrix $\boldsymbol{M}$ linearly transforms the distribution functions to the moments as $|\boldsymbol{m}\rangle = \boldsymbol{M}|f\rangle$. The equilibrium moment $\boldsymbol{m^{eq}}$ is obtained as $|m^{eq}\rangle = \boldsymbol{M}|f^{eq}\rangle$ with

$$f_\alpha^{eq} = w_\alpha \left(\rho + \rho_0 \left[\frac{\boldsymbol{e}_\alpha \cdot \boldsymbol{u}}{c_s^2} + \frac{(\boldsymbol{e}_\alpha \cdot \boldsymbol{u})^2 - c_s^2 |\boldsymbol{u}|^2}{2c_s^4}\right]\right), \tag{2}$$

where $\boldsymbol{u}$ is the fluid velocity, and ρ is expressed as the sum of the constant and fluctuation values: $\rho = \rho_0 + \delta\rho$ [41]. The non-dimensional sound speed is $c_s/c = 1/\sqrt{3}$, and w_α is the weighted coefficient. The collision matrix $\hat{\boldsymbol{S}}$ is diagonal:

$$\begin{aligned} \hat{\boldsymbol{S}} \equiv diag(&0,0,0,0,s_4,s_5,s_5,s_7,s_7,s_7,s_{10},s_{10},s_{10},s_{13}, \\ &s_{13},s_{13},s_{16},s_{17},s_{18},s_{18},s_{20},s_{20},s_{20},s_{23},s_{23},s_{23},s_{26}). \end{aligned} \tag{3}$$

The set of relaxation parameters originally proposed by [7] is as follows:

$$\begin{aligned} &s_4 = 1.54, \quad s_5 = s_7, \quad s_{10} = 1.96, \quad s_{13} = 1.83, \quad s_{16} = 1.4, \\ &s_{17} = 1.61, \quad s_{18} = s_{20} = 1.98, \quad s_{23} = s_{26} = 1.74. \end{aligned} \tag{4}$$

In this study, we have revised the s_{10} value from the original value ($s_{10} = 1.5$) in order to improve the numerical stability for higher Reynolds number turbulent flows. It is noted that this modification is based on truncation error analysis of the lattice Boltzmann equation, and we have confirmed that this modification hardly affects the predictive results for moderate Reynolds number flows but can remove unphysical numerical oscillations emerging in the high Reynolds number flows.

To introduce the SGS eddy viscosity, the relaxation parameter components s_5 and s_7 are related to the effective viscosity:

$$\nu + \nu_{sgs} = c_s^2 \left(\frac{1}{s_5} - \frac{1}{2} \right) \delta t = c_s^2 \left(\frac{1}{s_7} - \frac{1}{2} \right) \delta t, \tag{5}$$

where ν and ν_{sgs} are the kinematic viscosity and SGS eddy viscosity. In this study, the SGS eddy viscosity is given by the shear-improved variant of the Smagorinsky model (SISM) [42]:

$$\nu_{sgs} = (C_s \Delta)^2 \left(S_{ij} S_{ij} - \overline{S}_{ij} \overline{S}_{ij} \right), \tag{6}$$

where C_s is the Smagorinsky constant, S_{ij} is the strain tensor, and $\overline{S}_{ij}$ is averaged strain tensor. This model does not include any adjustable constant besides the standard Smagorinsky constant $C_s = 0.16$, and the wall-limiting behavior of the SGS eddy viscosity in the vicinity of the wall is satisfied without any empirical damping function. The strain tensor S_{ij} is computed from the non-equilibrium distribution function as in [18], and the average in time for the averaged strain tensor $\overline{S}_{ij}$ is taken during run.

The term F_α is the external force term [43]:

$$F_\alpha = w_\alpha \rho_0 \left\{ \frac{\boldsymbol{e}_\alpha \cdot \boldsymbol{a}}{c_s^2} \left(1 + \frac{\boldsymbol{e}_\alpha \cdot \boldsymbol{u}}{c_s^2} \right) - \frac{\boldsymbol{a} \cdot \boldsymbol{u}}{c_s^2} \right\}, \tag{7}$$

where $\boldsymbol{a}$ is an acceleration rate. In the framework of the LBM, the turbulence pressure cannot be taken into account. Thus, the influence of the SGS turbulence energy, k_{sgs}, is explicitly introduced in the external force term as in [7]:

$$\boldsymbol{a} = \frac{\partial}{\partial x_j} \left(-\frac{2}{3} k_{sgs} \delta_{ij} \right), \tag{8}$$

where k_{sgs} is given by the double-filtered velocity with a filter length of 2Δ as in [44], and δ_{ij} is the Kronecker delta. [7] may be referred to for the equilibrium moments $\boldsymbol{m^{eq}}$, transformation matrix $\boldsymbol{M}$, and weighted coefficients w_α.

For the scaler fields, there are also several discrete velocity models and collision models as with the flow field models. In this study, we choose the D3Q19 discrete velocity model with the regularized non-equilibrium distribution function. The regularization procedure projects the non-equilibrium distribution function onto the Hermite polynomial, which greatly improves the accuracy and numerical stability [45, 28]. To further improve the numerical stability in higher Reynolds number turbulent flow, we introduce the other relaxation time for the higher order term. The time evolution of the internal energy distribution function is expressed as follows:

$$|g \ (\boldsymbol{x} + \boldsymbol{e}_\alpha \delta t, t + \delta t)\rangle = |g^{eq} \ (\boldsymbol{x}, t)\rangle \quad + \quad \left(1 - \frac{1}{\tau_{g1}} \right) |g_1^{'} \ (\boldsymbol{x}, t)\rangle$$

$$+ \quad \left(1 - \frac{1}{\tau_{g2}}\right) |g_2^{'}\ (\boldsymbol{x}, t)\rangle + |So\ (\boldsymbol{x}, t)\rangle, \tag{9}$$

where the notation $|g\rangle = (g_0, g_1, \cdots, g_{18})^T$, and $\boldsymbol{e}_\alpha$ represents the discrete velocity vectors. The terms g_α^{eq} is the equilibrium distribution function as follows:

$$g_\alpha^{eq} = w_\alpha T \left(1 + \frac{\boldsymbol{u} \cdot \boldsymbol{e}_\alpha}{c_s^2}\right), \tag{10}$$

where temperature is $T = \Sigma_\alpha g_\alpha$, and w_α is the weighting constant [28]. Here, the discrete velocity components are

$$[\boldsymbol{e}_0\ \boldsymbol{e}_1\ \boldsymbol{e}_2\ \boldsymbol{e}_3\ \boldsymbol{e}_4\ \boldsymbol{e}_5\ \boldsymbol{e}_6\ \boldsymbol{e}_7\ \boldsymbol{e}_8\ \boldsymbol{e}_9\ \boldsymbol{e}_{10}\ \boldsymbol{e}_{11}\ \boldsymbol{e}_{12}\ \boldsymbol{e}_{13}\ \boldsymbol{e}_{14}\ \boldsymbol{e}_{15}\ \boldsymbol{e}_{16}\ \boldsymbol{e}_{17}\ \boldsymbol{e}_{18}]/c$$
$$= \begin{bmatrix} 0 & 1 & 0 & 0 & -1 & 0 & 0 & 1 & -1 & -1 & 1 & 1 & 0 & -1 & 0 & 1 & 0 & -1 & 0 \\ 0 & 0 & 1 & 0 & 0 & -1 & 0 & 1 & 1 & -1 & -1 & 0 & 1 & 0 & -1 & 0 & 1 & 0 & -1 \\ 0 & 0 & 0 & 1 & 0 & 0 & -1 & 0 & 0 & 0 & 0 & 1 & 1 & 1 & 1 & -1 & -1 & -1 & -1 \end{bmatrix},$$

The terms $g_{1,\alpha}^{'}$ and $g_{2,\alpha}^{'}$ are the first-and second-order terms of the regularized non-equilibrium distribution function, respectively. Note that the zeroth-order terms of the regularized non-equilibrium distribution function $g_{0,\alpha}^{'}$ is zero and not shown here. The regularized non-equilibrium part of the distribution function is expressed as follows:

$$g_{1,\alpha}^{\prime} = w_\alpha \left[\frac{1}{1!} C_i^{(1)} H_{i,\alpha}^{(1)}\right], \qquad g_{2,\alpha}^{\prime} = w_\alpha \left[\frac{1}{2!} C_{ij}^{(2)} H_{ij,\alpha}^{(2)}\right]. \tag{11}$$

The Hermite expansion coefficients $C_i^{(1)}, C_{ij}^{(2)}$ and the Hermite polynomial $H_{i,\alpha}^{(1)}, H_{ij,\alpha}^{(2)}$ are

$$C_i^{(1)} = \sum_\alpha (g_\alpha - g_\alpha^{eq}) H_{i,\alpha}^{(1)}, \qquad C_{ij}^{(2)} = \sum_\alpha (g_\alpha - g_\alpha^{eq}) H_{ij,\alpha}^{(2)}, \tag{12}$$

$$H_{i,\alpha}^{(1)} = \frac{1}{c_\mathrm{s}} \xi_{\alpha i}, \qquad H_{ij,\alpha}^{(2)} = \frac{\xi_{\alpha i} \xi_{\alpha j}}{c_\mathrm{s}^2} - \delta_{ij}. \tag{13}$$

To recover the filtered energy equation, the relaxation time τ_{g1} for $g'_{1,\alpha}$ should be related to the effective thermal diffusivity as follows:

$$\Gamma + \Gamma_{sgs} = c_s^2 \left(\tau_g - \frac{1}{2} \right) \delta t. \tag{14}$$

where $\Gamma_{sgs} = \nu_{sgs}/Pr_t$ with Pr_t being the turbulent Prandtle number given as $Pr_t = 0.9$. The first order term $g'_{1,\alpha}$ is essential to recover the energy equation while the presence of the second-order term $g'_{2,\alpha}$ is unaffected by the resulting energy equation. This means that τ_{g1} should be τ_g, but the relaxation time τ_{g2} for $g'_{2,\alpha}$ is a tunable parameter. While [28] prescribe $\tau_{g2} = \tau_{g1}$, we empirically optimize this value as $\tau_{g2} = max(0.51, \tau_{g1})$ to ensure numerical stability in this study.

The heat source term So_α can be expressed as

$$So_\alpha = w_\alpha \frac{Q}{\rho_0 c_p} \delta t, \tag{15}$$

where Q is the heat source per volume, and c_p is the specific heat. See [28] for the detail of the D3Q19 regularized LBM and application examples for the turbulent heat transfer simulations.

3. Near-wall modeling

The wall-function approaches prescribe the wall shear stress at wall neighboring nodes instead of imposing the no-slip conditions to the wall where strong mean velocity gradient is present. Although there are many possible routes for modeling near-wall turbulence, this study chooses the most basic method, which simply relies on a quasi-analytical model. Although there exist many models that describe the inner-scaled tangential mean velocity profile over a smooth wall, this study employs the one proposed by [46]:

$$\frac{u^T}{u_\tau} = f_u(y^+) \quad = \quad 5.424\tan^{-1}\left(0.1198y^+ - 0.4880\right) + 0.434\log\left(\frac{(y^+ + 10.6)^{9.6}}{\left({y^+}^2 - 8.15y^+ + 86\right)^2} - 3.507\right) \tag{16}$$

where u^T is the tangential velocity, u_τ is the friction velocity, and $y^+ = u_\tau y/\nu$ is the inner-scaled distance from a wall with y being the distance from the wall. Provided that u^T, y and ν are given, the friction velocity can be obtained by solving the equation:

$$\frac{u^T}{u_\tau} - f_u\left(\frac{u_\tau y}{\nu}\right) = 0. \tag{17}$$

This equation can be numerical solved by Newton-Raphson method, and the wall shear stress τ_w is thus given as follows:

$$\tau_w = \rho u_\tau^2. \tag{18}$$

As for the heat transfer, the wall heat flux should be determined based on near-wall modeling and is can be obtained in a similar fashion. The inner-scaled mean temperature over a smooth wall can be given by [47]:

$$\frac{|\theta - \theta_w|}{t_\tau} = f_\theta(y^+, Pr) = Pry^+\exp(-\gamma) + \left[2.12\log\left(1 + y^+\right) + \left(3.85Pr^{1/3} - 1.3\right)^2 + 2.12\log(Pr)\right]\exp(-1/\gamma), \tag{19}$$

where Pr is the Prandtle number, θ is the temperature, θ_w is the wall temperature, and t_τ is the friction temperature defined as $q_w/(\rho c_p u_\tau)$ with q_w being the wall heat flux. The function γ is given as

$$\gamma = \frac{0.01\left(Pry^+\right)^4}{1 + 5Pr^3y^+}. \tag{20}$$

Since t_τ does not appear on the right-hand side of Eq.(19), the wall heat flux can be computed without iterative calculation as follows:

$$q_w = -\frac{\rho c_p u_\tau (\theta - \theta_w)}{f_\theta(y^+, Pr)} \tag{21}$$

For the wall-modeled large-eddy simulation by the Navier-Stokes solver, one of the most important problem to be addressed is so called "log-layer mismatch" in which the predicted mean velocity profile deviates from the log-law profile. [38] give a comprehensive review of this problem, and concluded that the LES was necessarily inaccurate in the first grid point from a wall resulting in an inaccurate input to the wall-function method, which was plausible explanation for the "log-layer mismatch". One solution to overcome the"log-layer mismatch" suggested by [38, 36] was to simply avoid using the information of the first grid point from a wall to evaluate the wall shear stress. Thus, we set the reference point for the input of the wall-function such that the numerical errors contained within the first grid point does not spoil the estimated wall shear stress.

Figure 1 illustrate the position of the reference point in this study. We define the outward pointing wall-normal vector toward the fluid phase $\vec{n}$ where the origin is located at the wall-neighboring point P_N as shown in the figure. The first crossing point between $\vec{n}$ and the grid face is defined as the reference point P_R. The advantage of this definition is to avoid using the information of the wall-neighboring point, and no extrapolation is required to complement the physical quantity at the reference point. Moreover, the interpolation of the physical quantity at the reference point does not aggravate the high parallel computing performance stemming from the nature of the LBM because the interpolation process only requires the information of the neighboring nodes of P_N. Then, the wall shear stress and wall heat flux are given by Eqs.(17) and (21), respectively, with the tangential velocity u_p^T and temperature θ_p at the reference point, and the normal distance from the wall y_p as shown in the Figure.

4. Near-wall treatment for the lattice Boltzmann

The wall-modeled simulation can be straightforwardly implemented for the conventional Navier-Stokes solvers including the finite volume method or finite difference method by simply replacing the wall shear stress by the differential approximation method for that by the wall-function method. In contrast, many difficulties however arise when it comes to the implementation on the LBM. What we have to do is not only introducing the wall shear stress given by the wall-function but also prescribing all unknown particle distribution function components propagating from the wall. In the previous studies, [39] constructed the unknown particle distribution function based on the prescribed velocity and pressure while [40] employed the bounce-back method with the wall slip velocity evaluated by the wall-function. In this study, we first propose the specular reflection bounce-back method. The specular reflection imposes the zero wall shear stress condition with the mass and momentum conservation laws satisfied. Hence, it is possible to accurately introduce the modeled wall shear stress by applying the specular reflection for the unknown distribution components and adding the effect of the modeled wall shear stress on the external body force. This approach works quite well as demonstrated in §5; however, there is significant difficulties in applying this method to a curvilinear wall. To overcome this difficulties and increase an applicability, the alternative approach which assumes the immersed virtual wall is proposed. The following subsections describe the details of the two approaches.

4.1. Wall-function with specular reflection conditions

In this subsection, we describe the implementation method based on the specular reflection. This approach prescribe the unknown distribution function by assuming the fully slip wall conditions. In other words, the zero-wall shear stress is assumed for computing the unknown distribution function. When the slip wall is located at the midpoint between the fluid and solid nodes as shown in Fig.2, the unknown components f_α are given as follows:

$$f_\alpha(\boldsymbol{x} + \boldsymbol{e}_\gamma \delta t, t + \delta t) = \tilde{f}_\beta(\boldsymbol{x}, t), \tag{22}$$

where $\tilde{f}$ is the post collision distribution function, α and β satisfy the following relation: $\boldsymbol{e}_\beta = \boldsymbol{e}_\alpha - 2(\boldsymbol{e}_\alpha \cdot \boldsymbol{n})\boldsymbol{n}$, and $\boldsymbol{e}_\gamma = (\boldsymbol{e}_\alpha + \boldsymbol{e}_\beta)/2$. The wall shear stress estimated by the wall-function method is introduced in the lattice Boltzmann equation (1) as the external body force. The acceleration rate $\boldsymbol{a}$ in Eq. (7) can be written as:

$$\boldsymbol{a} = -\frac{A}{\rho_0 V}\boldsymbol{\tau}_w \tag{23}$$

where τ_w is the wall shear stress obtained by Eq.(17), A is the wall-facing area, and $V = \Delta^3$ is the volume of the cell. Since this approach imposes the fully-slip boundary conditions but adding the effects of the wall shear stress as the external force, the force offered by the wall is only the wall shear stress estimated by the wall-function. However, as the discrete velocity vector components are limited to the diagonal or aligned to the Cartesian grid, the specular reflection can be expressed only for the case where a wall is aligned to the Cartesian grid. Moreover, when we consider a wall with any inclination angle, the specularly reflected distribution function does not always stream to the neighboring node points. Hence, the formulation described in Eq. (22) is valid only for the case where the wall boundary is aligned with the Cartesian coordinate. Thus, the application of the present approach is limited to flow in considerably simple geometries. Considering an extension of this approach for curved boundaries or planar walls with any inclination angle is not straightforward, we do not go into the extension of this approach but concentrate on the development of the alternative approach as described in the following subsection.

4.2. Wall-function with immersed virtual wall method

The concept of the immersed virtual wall method is similar to the specular reflection condition: this method does not impose the no-slip boundary conditions at the wall but assumes a few virtual fluid nodes inside the wall. The lattice Boltzmann equation (Eq.1) is seamlessly solved in the virtual fluid nodes as in the other fluid node. Hence, this method allows the tangential slip velocity and local transpiration through the wall resulting a non-zero Reynolds stress at the wall. Although the present method is novel in terms of assuming virtual fluid nodes in the wall, the introduction of the slip velocity is a common idea for the implementation of the wall-function [48, 37, 49, 40]. In particular, it is interesting to note that the dynamic slip boundary conditions, which allows tangential and wall-normal velocity at the wall as in the present method, could be theoretically derived from the filtered Navier-Stokes equation. In what follows, the details of the present implementation method is descried.

Figure 3 illustrates the conceptual idea of the immersed virtual wall (IVW) method. As shown in the figure, the virtual wall is immersed in the wall. The virtual nodes, P_V, located between the wall and virtual wall are treated as in the other fluid nodes, and no bounce-back rule is applied to the nodes neighboring to the wall P_N in the figure. On the other hand, for the nodes neighboring to the virtual wall P_V', the bounce-back rule is applied to impose the no-slip boundary conditions at the virtual wall. Note that the figure illustrates the situation of the virtual wall layer thickness $h_v = 2\Delta$; however, the virtual wall layer thickness can be arbitrarily determined (the effect of h_v will be discussed in §5.4). To correctly introduce the wall shear stress evaluated by the wall-function, the additional body force is exerted to the nodes neighboring to the wall P_N. First the hydrodynamic force per volume offered by the wall can be calculated as the momentum equation method at point P_N:

$$\boldsymbol{F}^{M.E} = -\frac{1}{\delta t}\sum_{\beta}\left[\boldsymbol{e}_\beta f_\beta(\boldsymbol{x},t) - \boldsymbol{e}_\alpha \tilde{f}_\alpha(\boldsymbol{x},t)\right], \tag{24}$$

where $\boldsymbol{e}_\beta$ denotes the direction coming into the fluid node from the wall nodes, and $\boldsymbol{e}_\alpha = -\boldsymbol{e}_\beta$. Since the hydrodynamic force evaluated in Eq.(24) includes the pressure drag and viscous force, the viscous force $\boldsymbol{F}_v^{M.E}$ can be computed by eliminating the pressure drag effect from $\boldsymbol{F}^{M.E}$:

$$\begin{aligned}\boldsymbol{F}_v^{M.E} &= -\frac{1}{\delta t}\sum_{\beta}\left[\boldsymbol{e}_\beta\left(f_\beta - \frac{p}{c_s^2}\right) - \boldsymbol{e}_\alpha\left(\tilde{f}_\alpha - \frac{p}{c_s^2}\right)\right] \\ &= \boldsymbol{F}^{M.E} + \frac{1}{\delta t}\sum_{\alpha}\frac{p}{c_s^2}\omega_\alpha\left(\boldsymbol{e}_\beta - \boldsymbol{e}_\alpha\right), \end{aligned}\tag{25}$$

where $p = \rho c_s^2$ is the pressure. The additional acceleration rate is introduced to correct the viscous force offered by the wall by replacing the viscous force

$\boldsymbol{F}_v^{M.E}$ with the modeled wall shear force evaluated by the wall-function:

$$\boldsymbol{a} = -\frac{\boldsymbol{F}_v^{M.E}}{\rho_0} - \frac{A}{\rho V}\boldsymbol{\tau}_w \tag{26}$$

It is noted that the viscous force, $\boldsymbol{F}_v^{M.E}$, sometimes shows unphysical oscillation in space and time when evaluated in complex curved boundary as reported by [50]. Since this oscillation makes computation unstable and sometimes spoils the results, this study employs the filtered value in time and space to reduce the oscillation where, in practice, $\boldsymbol{F}_v^{M.E}$ is averaged over neighboring nodes and time during the run. Although it is rather ad hoc, it is also effective to set the threshold values for $\boldsymbol{F}_v^{M.E}$ to stabilize the computation.

For the thermal fields, the adiabatic boundary conditions [51] are applied to the nodes neighboring the virtual wall, P'_V, and the wall heat flux evaluated by the wall-function method in Eq.(21) is introduced to P_N, as the heat source per volume Q:

$$Q = q_w \frac{A}{V}. \tag{27}$$

This term is introduced to the lattice Boltzmann equation via the heat source term So_α in Eq.(15). This process accurately gives the wall heat flux evaluated by the wall-function without applying any bounce-back rules to the point P_N nor constructing the distribution function of P_N.

5. Turbulent channel flow simulation

This section provides validation of the above described approaches in the turbulent channel flow: one is the wall-function with the specular reflection conditions (case SR), and the other is that with the immersed virtual wall conditions (case IVW). Fig.4 shows the geometry of the turbulent channel flow. The computational domain was $6\delta(x) \times 2\delta(y) \times 3\delta$ in the streamwise, wall-normal, and spanwise direction, respectively, where δ is the half channel height. The flow was driven by a streamwise pressure difference, and the periodic boundary conditions were applied to the streamwise and spanwise directions. The friction Reynolds number $\mathrm{Re}_\tau = u_\tau\delta/\nu$ was varied to $\mathrm{Re}_\tau = 500, 5200, 10000$. To evaluate the grid dependency, the grid points across the half-channel height were changed from $NY = 20$ to $NY = 40$ points. In addition, to evaluate the effects of the thickness of the immersed virtual wall layer below the wall, the dependence of the IVW thickness h_v was evaluated by varying h_v from $h_v = \Delta$ to $h_v = 3\Delta$. For the turbulent heat transfer, the walls were heated by a uniform heat flux, and the Prandtl number was varied from 0.1 to 1000 in order to evaluate the applicability of the developed method for several Prandtl number flows. It should be noted that all the simulations except for the grid dependency test and the IVW thickness dependency test, the simulations were performed under the condition of $NY = 30$ and $h_v = 1.5\Delta$. Although we can choose arbitrary values of the kinematic viscosity and thermal diffusivity in the virtual node, the kinematic viscosity and thermal diffusivity in this study were assumed to be the same as those of the fluid phase.

5.1. Comparison of between the SR and IVW methods

Figure 5 shows a comparison of the inner-scaled mean velocity, $U^+ = \overline{u}/u_\tau$, predicted by SR and IVW, together with the DNS data from [52] at $\mathrm{Re}_\tau = 5200$. Here, overbar denotes the time average, and the friction velocity u_τ for normalization is computed from the streamwise pressure gradient.

Although the IVW method slightly underpredicts the mean velocity, the streamwise mean velocity profiles predicted by the SR and IVW show good agreement with the DNS data. This indicates that both the SR and IVW methods accurately introduce the wall shear stress by the wall-function to LBM.

Comparisons of the Reynolds shear stress, $-R_{12}$, is presented in Fig.6 where the SGS component, $2\nu_{SGS}\overline{S_{12}}$, and the sum of the grid-scale (GS) and SGS components, $-\overline{u'v'} + 2\nu_{SGS}\overline{S_{12}}$, are presented. Here, ϕ' denotes the fluctuation from the mean value ϕ. Figure 6 confirms that the SGS component considerably contributes at the few grid points off the wall for both cases, suggesting that turbulence near the wall is highly under-resolved. Away from the wall $0.2 < y/\delta < 1.0$, the predicted results for both cases are close to each other, and the sum of the GS and SGS components agrees well with the DNS data. However, when we focus on the profiles near wall region of $0 < y/\delta < 0.2$, a clear difference between the cases SR and IVW can be observed. The profile of the SGS component for case IVW is smooth and larger whereas that for case SR exhibits oscillation in the region. In addition, the sum of the GS and SGS components for case SR is significantly decayed at the first grid point off the wall. The reduction in the Reynolds shear stress at the first grid can be attributed to the reduction in the velocity fluctuations as shown in Fig.7. Figure 7 confirms that the Reynolds stress components of R_{11} and R_{22} away from the wall $0.2 < y/\delta$ for both cases are close and agree well with the DNS data. In contrast, when the attention is focused on the profiles near the wall, the profiles of R_{22} and R_{11} for both cases are significantly smaller than the DNS results.

The above discussions suggest that the SR provides a reasonably good performance for predicting turbulent flows over the wall. However, as mentioned earlier, the application of the SR method is limited to the case where the wall boundary is aligned with the Cartesian coordinate. Hence, in what follows, we concentrate on the evaluation of the performance of the IVW method.

5.2. Grid dependency

This subsection provides the discussion of the grid dependence of the IVW method on the solutions. Figure 8 shows profiles of the predicted mean velocity and Reynolds shear stress for different grid cases ($NY = 20, 30$ and 40) at $\mathrm{Re}_\tau = 5200$. Despite the considerable difference in the distance from the wall to the first grid point ($y_{p1}^+ = 260(NY = 20), y_{p1}^+ = 180(NY = 30), y_{p1}^+ = 130(NY = 40)$), Fig.8(a) shows that the developed method yields grid independent solutions for the mean velocity profiles. The sum of the GS and SGS Reynolds shear stress profiles in Fig.8(b) are also grid independent except the first grid point off the wall, and the predicted results are in excellent agreement with the DNS data from [52].

5.3. Reynolds number dependency

To evaluate the ability of the IVW method to correctly reproduce the Reynolds number dependency, profiles of the mean velocity and Reynolds shear stress at different friction Reynolds numbers of $\mathrm{Re}_\tau = 500$ and $10,000$ are presented in Fig.9. For comparison, also shown for the Musker law in Eq. (16) in Fig.9(a,b) and analytical solution for the total shear stress profile in Fig.9(c.d). Since the number of grid points across the half-channel height is fixed to $NY = 30$, the grid resolutions in wall units at $\mathrm{Re}_\tau = 500$ and $10,000$ are $\Delta^+ = 17$ and $\Delta^+ = 340$, respectively.

Figure 9 (a,b) demonstrates that the developed IVW method generally predicts the mean velocity at lower Re_τ case, whereas a slight log-layer mismatch can be found for the case with $\mathrm{Re}_\tau = 10,000$. One possible reason for the log-layer mismatch is the presence of the truncation error terms in the lattice Boltzmann equation (LBE). Unlike the Navier–Stokes solvers, the LBM does not directly solve the conservation laws of mass and momentum, but it solves the LBE in which the truncation error terms that violate the conservation laws are included. Therefore, changing the reference point, which is usually employed for the Navier–Stokes solver, does not completely resolve this problem. Alternatively, changing the collision operator may be a promising solution to resolve the log-layer mismatch [40], because the behavior of the truncation error terms depends strongly on the choice of the collision operator.

The Reynolds number dependence on the SGS and GS Reynolds shear stresses can be found in Fig.9(c,d). The SGS Reynolds shear stress at $\mathrm{Re}_\tau = 500$ in Fig.9(c) is much smaller than that at $\mathrm{Re}_\tau = 10,000$ in Fig.9(d), and the sum of the GS and SGS components at $\mathrm{Re}_\tau = 500$ in Fig.9(c) largely deviates from the total shear near the wall due to the role of the viscous shear stress. In contrast, when the Reynolds number is increased to $\mathrm{Re}_\tau = 10,000$, the SGS Reynolds shear stress as shown in Fig.9(d) accounts for half of the Reynolds shear stress, meaning that turbulence near the wall is substantially under-resolved at $\mathrm{Re}_\tau = 10,000$. Also, since the viscous effect is confined in the immediate vicinity of the wall, the sum of the GS and SGS Reynolds shear stress almost follows the total shear stress profile as shown in Fig.9(d).

5.4. Effects of the virtual wall layer thickness

The key point of the IVW method is the presence of a virtual wall layer that allows flow inside the wall and alleviates the prohibitive requirement of the grid resolution in the inner layer. However, it is expected that the thickness of the virtual wall layer affects the predictive accuracy. Hence, this subsection assesses the effect of the thickness of the virtual wall layer on the simulation results. Figure 10 shows the predicted mean velocity profiles and Reynolds shear stress around the wall by varying the thickness of the virtual wall layer to $h_v = \Delta$, 2Δ and 3Δ. It is noted that the friction Reynolds number is fixed at $\mathrm{Re}_\tau = 5200$ and the number of grid point across the half boundary layer is $NY = 30$.

Figure 10 (a) confirms that the virtual wall layer thickness h_v affects the mean velocity and its gradient at the reference point (i.e., the second grid point off the wall in this case). As h_v increases, the mean velocity at the reference point tends to be close to the DNS result, whereas the slope of the mean velocity at this point tends to decrease. Consequently, away from the wall $300 < y^+$, the profiles of U^+ for cases $h_v = \Delta$ and $h_v = 2\Delta$ collapse each other, whereas that for case $h_v = 3\Delta$ is somewhat lower than those for cases $h_v = \Delta$ and $h_v = 2\Delta$. The decrease in the slope of U^+ is associated with the enhanced Reynolds shear stress at the wall due to an increase in the tangential slip velocity and local transpiration through the wall with h_v. This can clearly be found in Fig.10 (b) where the sum of the GS and SGS Reynolds shear stress and its SGS component are plotted. The SGS Reynolds shear stress at the wall decreases as h_v increases; however, the enhanced tangential and wall-normal slip velocity increases the GS Reynolds shear stress. As a result, the sum of the GS and SGS components at the first grid point off the wall increases with h_v.

It should be stressed that although the results are not shown here, the solution does not converge when we further thicken the virtual wall layer thickness. This is because the non-zero Reynolds shear stress at the wall progressively increases with h_v, decreasing the slope of U^+. This subsection confirms that the appropriate slip velocity that yields reasonable solutions can be achieved when the virtual wall layer thickness is $\Delta - 2\Delta$. Although the ideal value for h_v may depend on the flow conditions, we use $h_v = 1.5\Delta$ throughout this work. Exploring the ideal value will be left for future work.

5.5. Thermal field predictions

The above subsections evaluate the predictive accuracy of the wall-modeled LBM for the flow field while it should be stressed that the wall modeling is particularly important for high Prandtl number flow because the thermal boundary layer is progressively thinner as the Prandtl number increases and an enormous number of grid points is required to resolve the thermal boundary layer. This subsection demonstrates the potential of the developed IVW method for various Prandtl number flows. Figure 11 presents profiles of the inner-scaled mean temperature, $\overline{\theta^+}$, for various Prandtl number cases together with the profiles of Kader law in Eq. (19). Here, the friction temperature for the normalization is given as $t_\tau = q_w/(\rho c_p u_\tau)$. The figure confirms that the developed method provides a faithful account of the effect of the Prandtl number: the $\overline{\theta^+}$ profile at the low Prandtl number case $Pr = 0.1$ agrees well with the Kader profile as shown in Fig.11(b), and substantially increased $\overline{\theta^+}$ at the high Prandtl number case $Pr = 1000$ in Fig.11 is reasonably reproduced by the present method as well. The discrepancy with the Kader law is found to be within a few percent even for the highest Pr number case, where the thermal boundary layer is much thinner than the corresponding velocity boundary layer. These results suggest that the wall-function with the developed IVW method is capable of correctly predicting the thermal fields for various Prandtl number flows.

6. Circular pipe flow simulation

The previous section provides the validation results for the turbulent channel flow where the wall boundary is aligned with the Cartesian coordinate. However, flow configuration in the engineering products usually have a complex curved wall, and it is essential for the engineering CFD tool to deal with a curvilinear wall. Thus, this section evaluates the performance of the developed IVW method in a fully-developed turbulent circular pipe flow. The domain length in the streamwise direction was $10D$, where D is the pipe diameter. To evaluate the grid dependency, we changed the grid resolution across the pipe diameter as $D/\Delta = 35.5, 50.5$, and 75.5 while the thickness of the virtual wall layer was fixed to $h_v = 1.5\Delta$. The flow was driven by a streamwise pressure difference, and the periodic boundary conditions were imposed in the streamwise directions. The Reynolds number based on the pipe diameter and bulk mean velocity ranged from $Re_D = 1.0 \times 10^4$ to 1.0×10^6. The Prandtl number 0.71 was used assuming an air flow, and the wall was heated by a uniform heat flux.

Figure 12 shows a comparison of the friction factor f and Nusselt number Nu with the experimental correlations $f = 0.3164 Re_D^{-0.25}$ ($Re_D < 10^5$) by [53], $1/\sqrt{f} = 2.0\log\left(Re_d\sqrt{f}\right) - 0.8$ ($10^5 < Re_D$) by [54], and $Nu = 0.023 Re^{0.8} Pr^{0.4}$ by [55]. First when we take a closer look at Fig.12(a), it is found that the predicted f is somewhat overpredicted particularly for the high Reynolds number flow at 1.0×10^6, e.g., f is 22% overpredicted when $\mathrm{Re}_D = 10^6$ and $D/\Delta = 50.5$. It is also found that the grid convergence of f is worse than that of Nu. However, Fig.12 confirms that f and Nu generally accord with the experimental correlation from $Re = 1.0 \times 10^4$ to 1.0×10^6, suggesting that the wall-function with the developed IVW method has a potential to deal with the curved boundary with satisfactory accuracy for a wide range of the Reynolds number.

7. Channel with streamwise periodic hill

Finally, to demonstrate the performance of the developed IVW method for complex flow simulations, this section provides validation in a turbulent channel with streamwise periodic constrictions where the flow is characterized by separation and reattachment due to a two-dimensional hill. This flow configuration is frequently chosen for the validation test of the wall-modeled LES since this validation test evaluate the ability of the wall-function to correctly predict the wall shear stress in the complex flow geometry. The flow geometry of a periodic hill flow is shown in Fig.13 which is identical to that employed in the wall-resolved LES study of [56]. The size of the computational domain was $L_x = 9h$, $L_y = 3.04h$, $L_z = 4.5h$ in the streamise, vertical, and spanwise direction, respectively, where h is the height of the construction. The periodic boundary conditions were applied to the streamwise and spanwise directions, the wall-function was used for the walls located at $y/h = 3.04H, 0.0$ and the surface of the hill. The virtual wall layer thickness was $h_v = 1.5\Delta$, and the grid points including the virtual wall layer region was $252(x) \times 89(y) \times 126(z)$. The Reynolds number based on the bulk mean velocity at the hill crest, U_h, and the hill height was $\mathrm{Re}_h = 10500$. The pressure difference imposed between the outlet and inlet boundary was adjusted so as to yield the desired flow rate. The predicted results were compared with the resolved LES results in the ERCOFTAC database. In the reference resolved LES, the dynamic Smagorinsky model was used, and wall-function approach was adopted at the upper wall. [56] may be referred to for details of the resolved LES.

A contour map of the streamwise mean velocity with the steramlines is presented in Fig.14. It is observed that a flow separation is occurred near the hill crest generating a recirculation flow behind the hill crest. The reattachment point is predicted at $x = 4.4h$, which is fairly close to the reference data of $x = 4.72h$ despite the fact that the reattachment point is considerably sensitive to the wall-treatment and SGS models.

First, to assess the validity of the present wall treatment, Fig.15 shows a comparison of the skin friction coefficient, C_f, at the bottom surface with the LES data from [57]. There is a considerable geometry-induced spatial variation in the C_f value: C_f is negative in the backflow region behind the hill of $1 < x/h < 4.5$, whereas it dramatically increases in the region of $7 < x/h < 9$ owing to the flow contraction by the hill. This trend is reasonably captured by the present method, and the predicted C_f is generally close to the reference LES data. However, the negative absolute C_f value in the backflow region is underpredicted, and the rapid increase in the C_f value toward the hill crest of is not perfectly reproduced. Note that although the simulated Reynolds number is not sufficiently high to evaluate the performance of the wall-function, the grid resolution in wall unit based on the friction velocity at the bottom surface is 13 on average with its maximum value of 48, suggesting that the near-wall turbulent flow is underresolved in the present grid resolution. The present grid resolution is coarser than that employed in the study on the wall-modeled LES of the periodic hill flows by [56] where the near-wall modeling plays an important role in predicting the general flow field.

The predicted streamwise and vertical mean velocity profiles at different streamwise locations $x/h = 1, 2, 4, 6$ and 8 are compared in Fig.16. In Fig.16(a), the general agreement of the streamwise mean velocity with the reference is satisfactory. The reversal mean flow behind the hill crest at $x/h = 1$ and 2 and the recovery of the reversal flow at $x/h = 4$ and 6 are reasonably captured by the present method. However, the predicted back flow at $x/h = 2$ is slightly weak relative to the reference data. The discrepancy in the backflow region can also be confirmed in the C_f profile in Fig. 15. Near the top wall, the present method produces a small kink profile in the streamwise mean velocity at $x/h = 4$ and 6, which may stem from the fact that the present wall-function assumes the mean velocity profile in the equilibrium boundary layer. It should be noted that although the results are not shown here, the mean velocity at the reference point near the top wall is confirmed to match the solution of the profile in Eq.(16). As for the vertical mean velocity profile as shown in Fig.16(b), the present method reasonably captures the trend of the resolved LES results. The small discrepancy observed near the hill at $x/h = 1, 2$ and 8 may be due to the use of the log-law based wall-function, and can be reduced by introducing more elaborate wall-function models [58, 59, 60] that can deal with flow separation and reattachment. Finally, the predictive results of the streamwise Reynolds stress are compared in Fig.17. Although the present method underepredicts the streamwise Reynolds stress behind the hill at $x/h = 2$ and 4, the general agreement with the resolved LES data is satisfactory. This demonstrates that the immersed virtual wall method successfully incorporates the LBM with the wall-function, and the wall-modeled LBM with the IVW method can be a promising CFD tool for dealing with high Reynolds number flows in complex geometries.

8. Conclusions

The implementation issue of the wall-function method to the LBM is discussed to extend the applicability of the LBM for high Reynolds number turbulent heat transfer in complex geometries. We consider two implementation strategies: specular reflection and immersed virtual wall methods. The specular reflection method gives the distribution functions propagating from the solid node based on the specular reflection rule, while the immersed virtual wall method assumes the virtual wall layer beneath the wall which satisfies the slip wall conditions allowing the subsurface heat and fluid to flow within the solid wall. The D3Q27 multiple-relaxation-time LBM and D3Q19 regularized LBM are used to simulate flow and scaler fields, respectively, and the standard log-law based wall-function method is used. The validation test in turbulent channel flows suggests that the developed methods yield a grid-independent solution with satisfactory accuracy. Moreover, the immersed virtual wall method is confirmed to be applied in highly underresolved conditions and has great potential for predicting high Prandtl number flow. The advantage of the immersed virtual wall method over the specular reflection method is its applicability to a complex curvilinear wall. To assess this advantage, the immersed virtual wall methods were further validated against turbulent flows in a circular pipe and channel with two-dimensional constraints. This confirms that the immersed virtual wall method can successfully deal with complex curvilinear walls.

The accuracy of this method may be further improved by using the other collision models that can reduce the effects of the truncation error terms or optimizing the value for the virtual wall layer thickness. Furthermore, introduction of more elaborate non-equilibrium wall-function methods and further validation studies in other complex geometries make the LBM much better for the engineering computational fluid dynamic tool.

Acknowledgements

The authors express their gratitude to Dr. M. Kaneda for his support and thank Dr. B. Basara of AVL List GmbH Graz for the discussion on the model validation of turbulent heat transfer. The numerical calculations were carried out on the TSUBAME3.0 supercomputer in the Tokyo Institute of Technology in a research project (ID : hp190013).

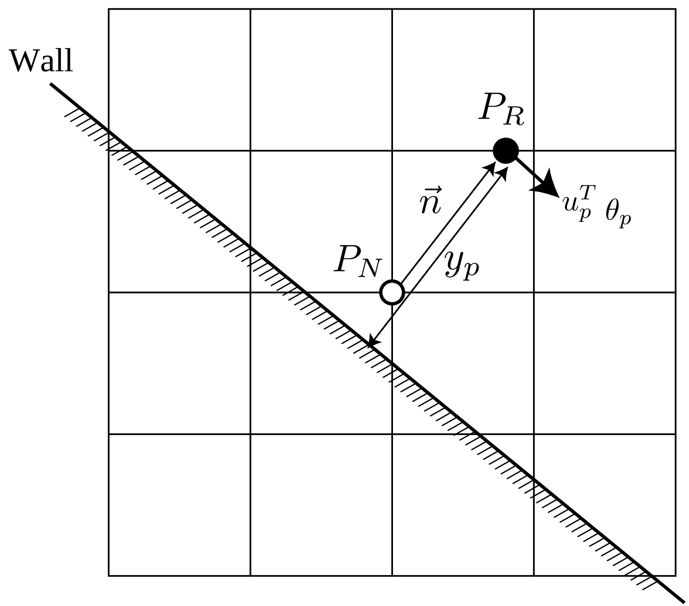

Figure 1: Reference point P_R for the wall-function method.

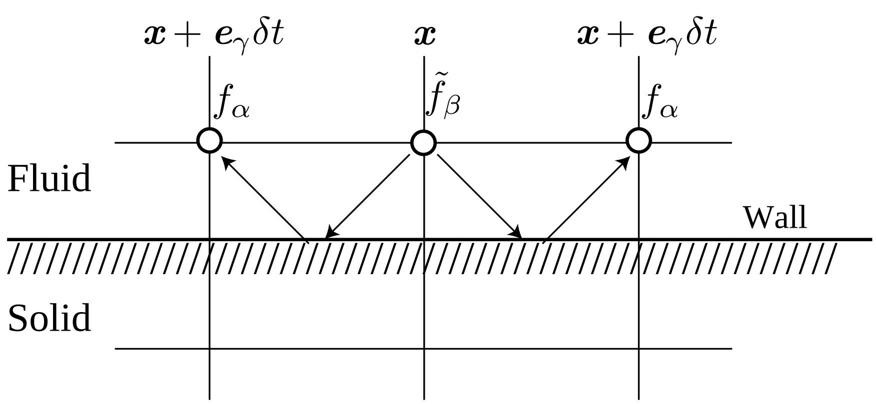

Figure 2: Specular reflection rule.

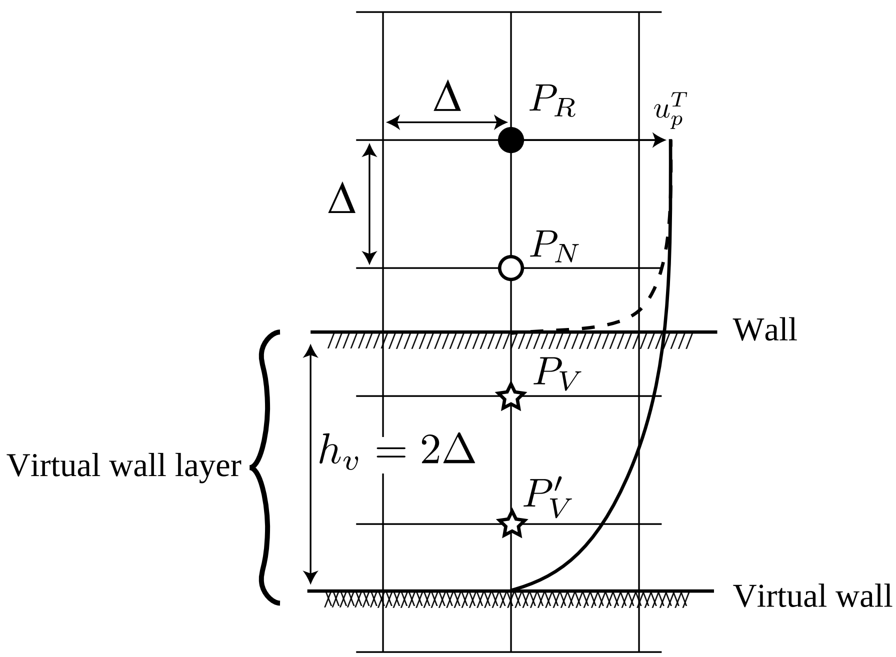

Figure 3: Near wall node points for the immersed virtual wall method: P_R is the reference point for the wall-function, P_N is the node neighboring to the wall, P_V is the virtual node, and P_V' is the nodes neighboring to the virtual wall. The solid and broken lines are respectively the actual velocity profile and approximated profile by the wall-function.

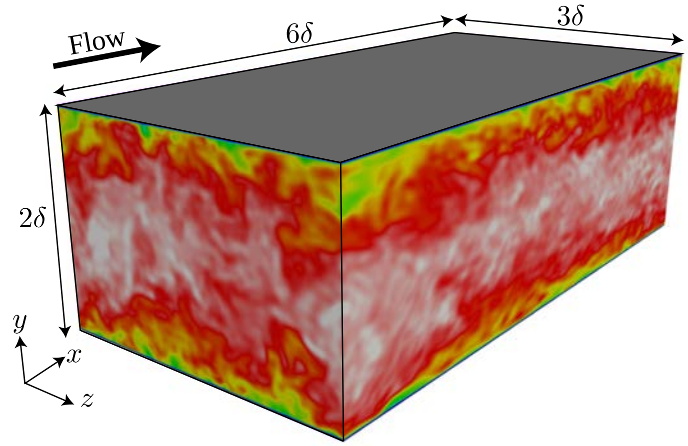

Figure 4: Computational domain of a turbulent channel flow.

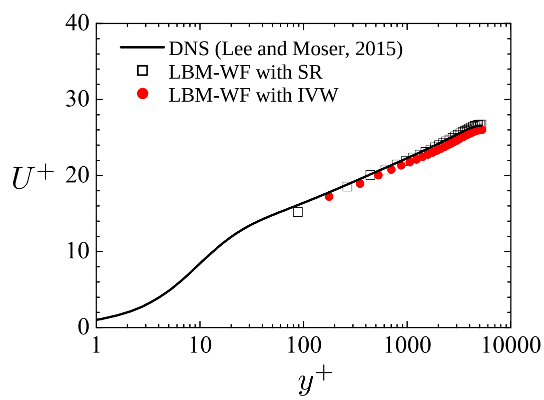

Figure 5: Comparison of the streamwise mean velocity profile with the DNS data from [52].

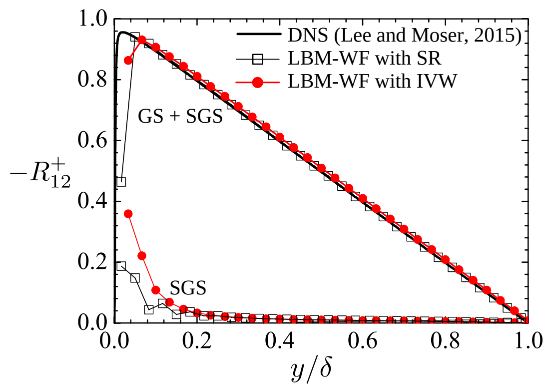

Figure 6: Comparison of the Reynolds shear stress profile with the DNS data from [52]: the SGS (modeled) component, $2\nu_{SGS}S_{12}$, and the sum of the GS (resolved) and SGS components, $-\overline{u'v'} + 2\nu_{SGS}S_{12}$, are presented.

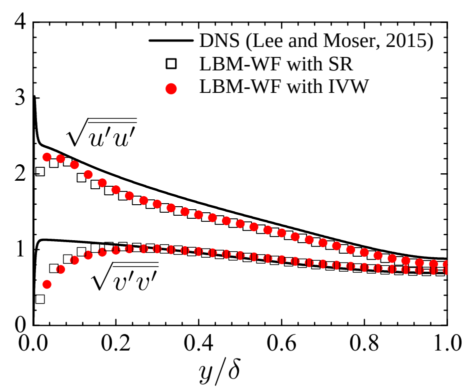

Figure 7: Comparison of the streamwise and wall-normal Reynolds stresses with the DNS data from [52].

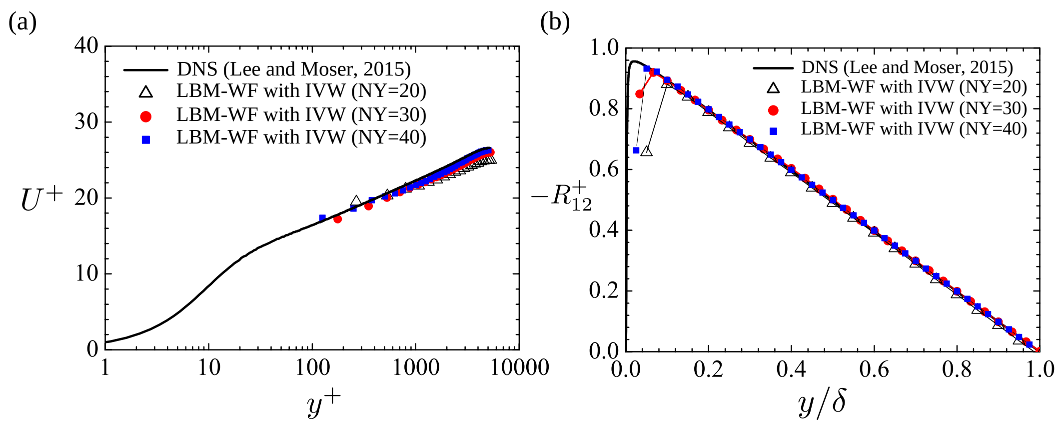

Figure 8: Grid dependence on the predictive results: (a) streamwise mean velocity and (b) sum of GS and SGS Reynolds shear stress.

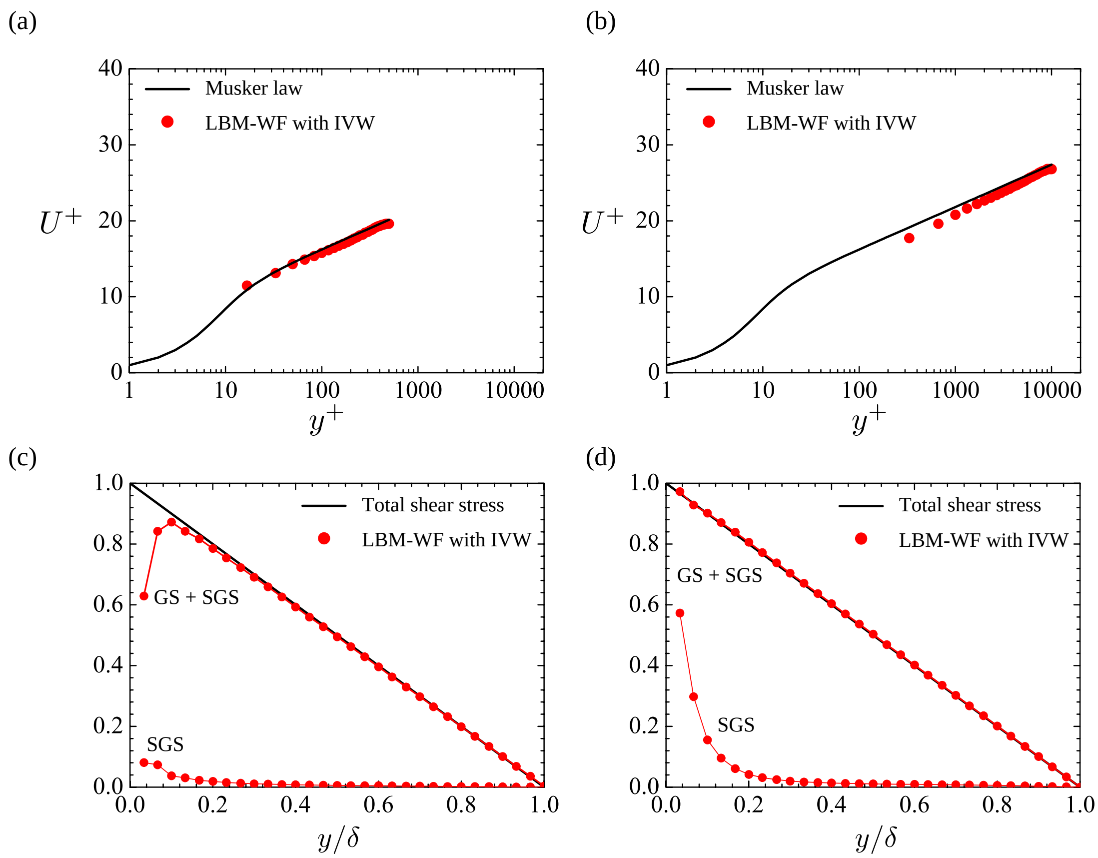

Figure 9: Comparison of the predictive results for different Re_τ: (a) streamwise mean velocity at $\mathrm{Re}_\tau = 500$, (b) streamwise mean velocity at $\mathrm{Re}_\tau = 10,000$, (c) Reynolds shear stress at $\mathrm{Re}_\tau = 500$, and (d) Reynolds shear stress at $\mathrm{Re}_\tau = 10,000$.

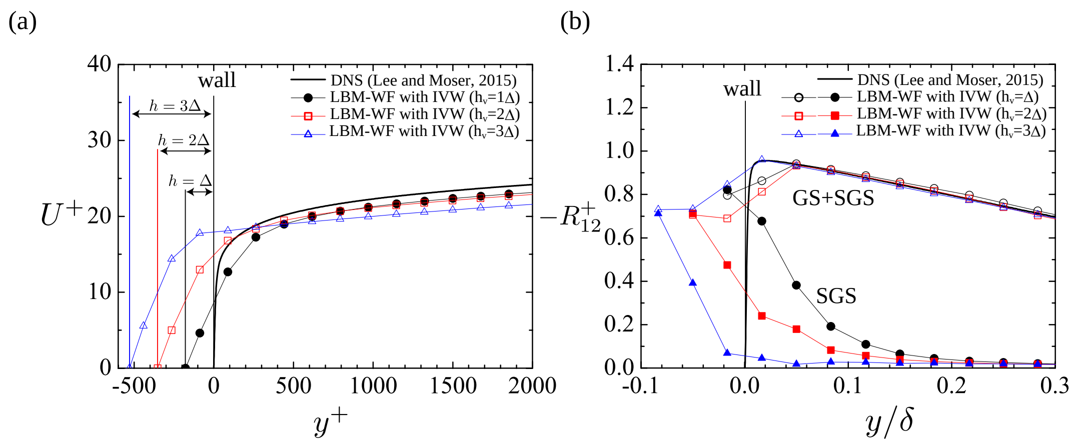

Figure 10: Effect of the virtual wall layer thickness on the predictive results: (a) streamwise mean velocity and (b) Reynolds shear stress profile.

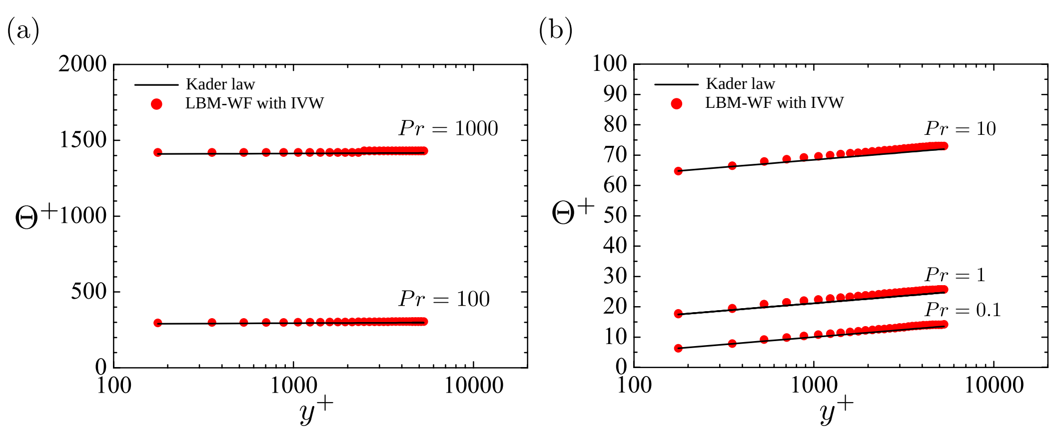

Figure 11: Comparison of the mean temperature profiles for different Prandtl number, (a) for $Pr = 1000$ and 100, (b) for $Pr = 10, 1.0$ and 0.1.

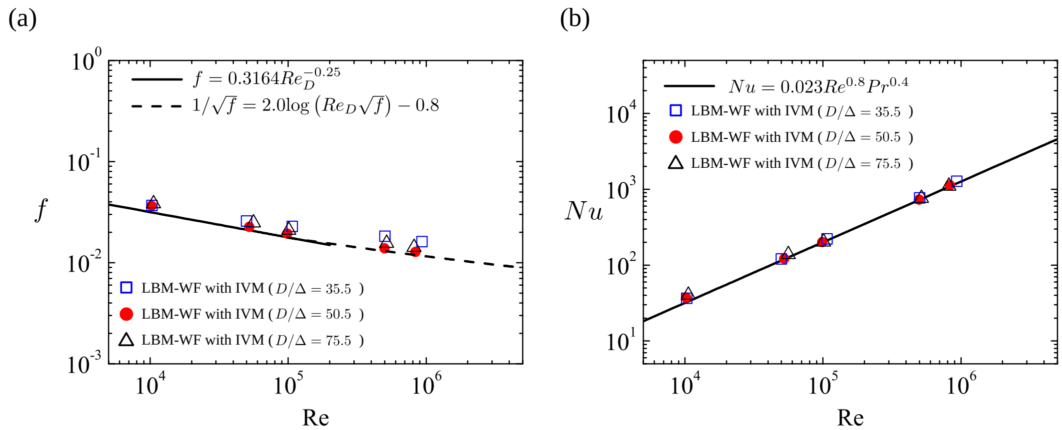

Figure 12: (a) comparison of the friction factor of the circular pipe with $f = 0.3164Re_D^{-0.25}$ ($Re_D < 10^5$) by [53], $1/\sqrt{f} = 2.0\log\left(Re_D\sqrt{f}\right) - 0.8$ ($10^5 < Re_D$) by [54], (b) Comparison of the Nusselt number of the circular pipe with $Nu = 0.023Re^{0.8}Pr^{0.4}$ by [55].

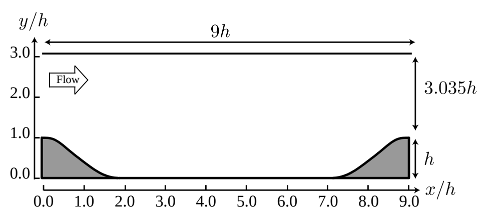

Figure 13: Computational geometry of channel with streamwise periodic hill.

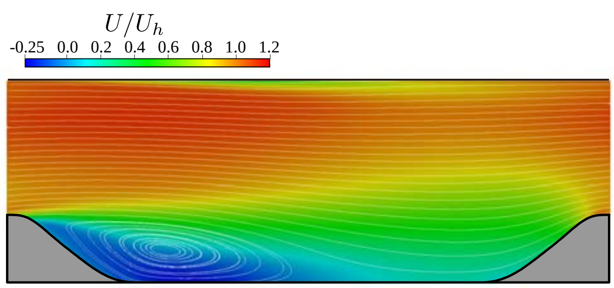

Figure 14: Contour map of the streamwise mean velocity with steramlines.

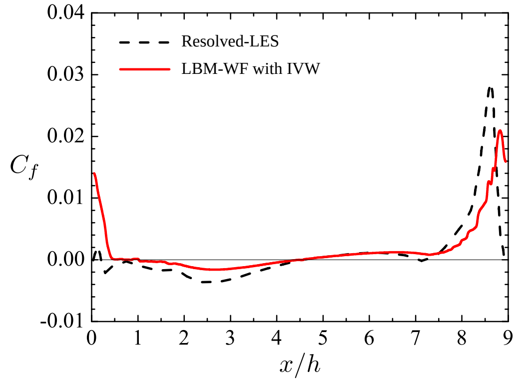

Figure 15: Comparison of the skin friction coefficient with the resolved LES data from [57].

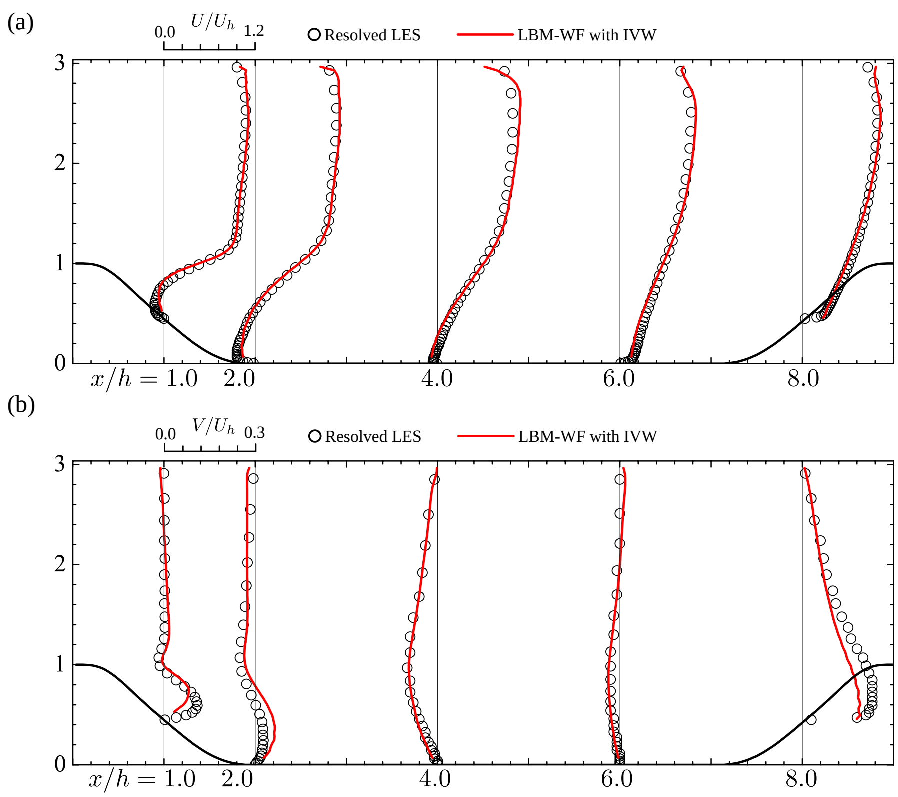

Figure 16: Comparison of the mean velocity profile with the resolved LES data from [56]: (a) Streamwise mean velocity and (b)vertical mean velocity.

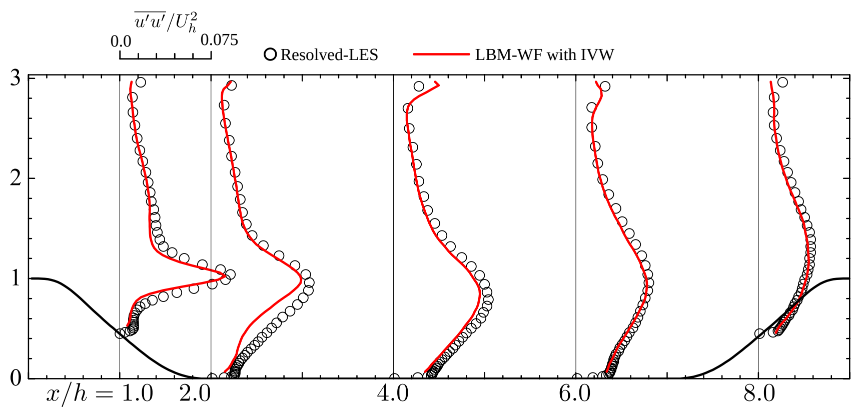

Figure 17: Comparison of the streamwise Reynolds stress profile with the resolved LES data from [56].

References

[1] C. Aidun, J. Clausen, Lattice-Boltzmann method for complex flows, Annu. Rev. Fluid Mech. 42 (2010) 439–472.

[2] X. Wang, T. Aoki, High Performance Computation by Multi-Node GPU Cluster-Tsubame2. 0 on the Air Flow in an Urban City Using Lattice Boltzmann Method, Int. J. Aero. Lightweight Struct. (IJALS) 2 (1).

[3] L. Xipeng, Z. Yun, W. Xiaowei, G. Wei, GPU-based numerical simulation of multi-phase flow in porous media using multiple-relaxation-time lattice Boltzmann method, Chem. Eng. Sci. 102 (2013) 209 – 219.

[4] N. Onodera, T. Aoki, T. Shimokawabe, H. Kobayashi, Large-scale LES wind simulation using lattice Boltzmann method for a 10 km$\times$ 10 km area in metropolitan Tokyo, TSUBAME e-Science J. Global Scientific Information and Computing Center 9 (2013) 1–8.

[5] C. Huang, B. Shi, N. He, Z. Chai, Implementation of Multi-GPU based lattice Boltzmann method for flow through porous media, Adv. Appl. Math. Mech. (2015) 1–12.

[6] D. d'Humieres, Multiple–relaxation–time lattice Boltzmann models in three dimensions, Phil. Trans. R. Soc. A 360 (1792) (2002) 437–451.

[7] K. Suga, Y. Kuwata, K. Takashima, R. Chikasue, A D3Q27 Multiple-Relaxation-time lattice Boltzmann method for turbulent flows, Comput. Math. Appl. 69 (2015) 518–529.

[8] P. Asinari, Generalized local equilibrium in the cascaded lattice Boltzmann method, Phys. Rev. E 78 (1) (2008) 016701.

[9] M. Geier, A. Greiner, J. Korvink, A factorized central moment lattice Boltzmann method, The Europ. Phys. J. Spe. Topics 171 (1) (2009) 55–61.

[10] M. Geier, M. Schönherr, A. Pasquali, M. Krafczyk, The cumulant lattice Boltzmann equation in three dimensions: Theory and validation, Comput. Math. Appl. 70 (4) (2015) 507–547.

[11] P. Lammers, K. Beronov, R. Volkert, G. Brenner, F. Durst, Lattice BGK direct numerical simulation of fully developed turbulence in incompressible plane channel flow, Comput. fluids 35 (10) (2006) 1137–1153.

[12] R. Freitas, A. Henze, M. Meinke, W. Schröder, Analysis of Lattice-Boltzmann methods for internal flows, Comput. Fluids 47 (1) (2011) 115–121.

[13] A. T. White, C. K. Chong, Rotational invariance in the three-dimensional lattice Boltzmann method is dependent on the choice of lattice, J. Comput. Phys. 230 (16) (2011) 6367 – 6378.

[14] S. K. Kang, Y. A. Hassan, The effect of lattice models within the lattice Boltzmann method in the simulation of wall-bounded turbulent flows, J. Comput. Phys. 232 (1) (2013) 100 – 117.

[15] Y. Kuwata, K. Suga, Anomaly of the lattice Boltzmann methods in three-dimensional cylindrical flows, J. Comput. Phys. 280 (2015) 563 – 569.

[16] B. Dorschner, F. Bösch, S. Chikatamarla, K. Boulouchos, I. Karlin, Entropic multi-relaxation time lattice Boltzmann model for complex flows, J. Fluid Mech. 801 (2016) 623–651.

[17] M. Gehrke, C. Janßen, T. Rung, Scrutinizing lattice Boltzmann methods for direct numerical simulations of turbulent channel flows, Comput. Fluids 156 (2017) 247–263.

[18] H. Yu, S. S. Girimaji, L.-S. Luo, DNS and LES of decaying isotropic turbulence with and without frame rotation using lattice Boltzmann method, J. Comput. Phys. 209 (2) (2005) 599–616.

[19] Ö. Ertunç, N. Özyilmaz, H. Lienhart, F. Durst, K. Beronov, Homogeneity of turbulence generated by static-grid structures, J. Fluid Mech. 654 (2010) 473–500.

[20] Y. Peng, W. Liao, L.-S. Luo, L.-P. Wang, Comparison of the lattice Boltzmann and pseudo-spectral methods for decaying turbulence: Low-order statistics, Comput. Fluids 39 (4) (2010) 568–591.

[21] F. Bösch, S. Chikatamarla, I. Karlin, Entropic multirelaxation lattice Boltzmann models for turbulent flows, Phys. Rev. E 92 (4) (2015) 043309.

[22] Y. Kuwata, K. Suga, Imbalance-correction grid-refinement method for lattice Boltzmann flow simulations, J. Comput. Phys. 311 (2016) 348–362.

[23] Y. Kuwata, K. Suga, Lattice Boltzmann direct numerical simulation of

interface turbulence over porous and rough walls, Int. J. Heat Fluid Flow 61 (2016) 145–157.

[24] Y. Kuwata, Y. Kawaguchi, Direct numerical simulation of turbulence over resolved and modeled rough walls with irregularly distributed roughness, Int. J. Heat Fluid Flow. 77 (2019) 1–18.

[25] Y. Kuwata, Y. Kawaguchi, Direct numerical simulation of turbulence over systematically varied irregular rough surfaces, J. Fluid Mech. 862 (2018) pp.781–815.

[26] Y. Kuwata, K. Suga, Extensive investigation of the influence of wall permeability on turbulence, Int. J. Heat Fluid Flow. 80 (2019) 108465.

[27] Y. N., Y. K., K. S., Direct numerical simulation of turbulent heat transfer over fully resolved anisotropic porous structures, Int. J. Heat Fluid Flow 81 (2020) 108515.

[28] K. Suga, R. Chikasue, Y. Kuwata, Modelling turbulent and dispersion heat fluxes in turbulent porous medium flows using the resolved LES data, Int. J. Heat Fluid Flow. 68 (2017) 225–236.

[29] Y. Kuwata, K. Suga, Large eddy simulations of pore-scale turbulent flows in porous media by the lattice Boltzmann method, Int. J. Heat Fluid Flow 55 (2015) 143–157.

[30] S. Lenz, M. Schoenherr, M. Geier, M. Krafczyk, A. Pasquali, A. Christen, M. Giometto, Towards real-time simulation of turbulent air flow over a resolved urban canopy using the cumulant lattice Boltzmann method on a GPGPU, J. Wind Eng. Ind. Aerod. 189 (2019) 151–162.

[31] H. Sajjadi, M. Salmanzadeh, G. Ahmadi, S. Jafari, Turbulent indoor airflow simulation using hybrid LES/RANS model utilizing lattice Boltzmann method, Comput. Fluids 150 (2017) 66–73.

[32] H. Yu, L.-S. Luo, S. Girimaji, LES of turbulent square jet flow using an MRT lattice boltzmann model, Comput. Fluids 35 (8-9) (2006) 957–965.

[33] S. Geller, S. Uphoff, M. Krafczyk, Turbulent jet computations based on MRT and Cascaded Lattice Boltzmann models, Comput. Math. Appl. 65 (12) (2013) 1956–1966.

[34] B. Launder, D. Spalding, The numerical computation of turbulent flows, Comput. Method Appl. Mech. Eng. 3 (2) (1974) 269 – 289.

[35] W. Cabot, P. Moin, Approximate wall boundary conditions in the large-eddy simulation of high reynolds number flow, Flow, Turb. Combust. 63 (1-4) (2000) 269–291.

[36] S. Kawai, J. Larsson, Wall-modeling in large eddy simulation: Length scales, grid resolution, and accuracy, Phys. Fluids 24 (1) (2012) 015105.

[37] S. Bose, P. Moin, A dynamic slip boundary condition for wall-modeled large-eddy simulation, Phys. Fluids 26 (1) (2014) 015104.

[38] J. Larsson, S. Kawai, J. Bodart, I. Bermejo-Moreno, Large eddy simulation with modeled wall-stress: recent progress and future directions, Mech. Eng. Rev. 3 (1) (2016) 15–00418.

[39] O. Malaspinas, P. Sagaut, Wall model for large-eddy simulation based on the lattice Boltzmann method, J. Comput. Phys. 275 (2014) 25–40.

[40] A. Pasquali, M. Geier, M. Krafczyk, Near-wall treatment for the simulation of turbulent flow by the cumulant lattice Boltzmann method, Comput. Math. Appl. 79 (1) (2020) 195–212.

[41] X. He, L.-S. Luo, Lattice Boltzmann model for the incompressible Navier-Stokes equation, J. Stat. Phys. 88 (3-4) (1997) 927–944.

[42] E. Lévêque, F. Toschi, L. Shao, J.-P. Bertoglio, Shear-improved Smagorinsky model for large-eddy simulation of wall-bounded turbulent flows, J. Fluid Mech. 570 (2007) 491–502.

[43] Z. Guo, C. Zheng, B. Shi, Discrete lattice effects on the forcing term in the lattice Boltzmann method, Phys. Rev. E 65 (4) (2002) 046308.

[44] M. Inagaki, M. Nagaoka, N. Horinouchi, K. Suga, Large eddy simulation analysis of engine steady intake flows using a mixed-time-scale subgrid-scale model, Int. J. Engine Res. 11 (2010) 229–241.

[45] J. Latt, B. Chopard, Lattice Boltzmann method with regularized pre-collision distribution functions, Math. Comput. Simulat. 72 (2-6) (2006) 165–168.

[46] A. Musker, Explicit expression for the smooth wall velocity distribution in a turbulent boundary layer, AIAA J. 17 (6) (1979) 655–657.

[47] B. Kader, Temperature and concentration profiles in fully turbulent boundary layers, Int. J. Heat Mass Transfer 24 (9) (1981) 1541–1544.

[48] J. Hoffman, Simulation of turbulent flow past bluff bodies on coarse

meshes using General Galerkin methods: drag crisis and turbulent Euler solutions, Comput. Mech. 38 (4-5) (2006) 390–402.

[49] R. Golshan, A. E. Tejada-Martínez, M. Juha, Y. Bazilevs, Large-eddy simulation with near-wall modeling using weakly enforced no-slip boundary conditions, Comput. Fluids 118 (2015) 172–181.

[50] R. Mei, D. Yu, W. Shyy, L.-S. Luo, Force evaluation in the lattice Boltzmann method involving curved geometry, Phys. Rev. E 65 (4) (2002) 041203.

[51] L. Li, R. Mei, J. Klausner, Boundary conditions for thermal lattice Boltzmann equation method, J. Comput. Phys. 237 (2013) 366–395.

[52] M. Lee, R. D. Moser, Direct numerical simulation of turbulent channel flow up to $re_\tau \approx 5200.$, J. Fluid Mech. 774 (2015) 395–415.

[53] H. Blasius, The Law of Similarity of Frictional Processes in Fluids, ForschArbeitIngenieur-Wesen, Berlin 131.

[54] L. Prandtl, W. Durand, Aerodynamic theory, iii, Div. G.

[55] F. Dittus, L. Boelter, Heat transfer in automobile radiators of the tubular type, Int.l Commu. Heat Mass 12 (1) (1985) 3–22.

[56] L. Temmerman, M. Leschziner, C. Mellen, J. Fröhlich, Investigation of wall-function approximations and subgrid-scale models in large eddy simulation of separated flow in a channel with streamwise periodic constrictions, Int. J Heat Fluid Flow 24 (2) (2003) 157–180.

[57] J. Fröhlich, C. Mellen, W. Rodi, L. Temmerman, M. Leschziner, Highly resolved large-eddy simulation of separated flow in a channel with streamwise periodic constrictions, J. Fluid Mech. 526 (2005) 19.

[58] S. Kawai, J. Larsson, Dynamic non-equilibrium wall-modeling for large eddy simulation at high reynolds numbers, Phys. Fluids 25 (1) (2013) 015105.

[59] G. I. Park, Wall-modeled large eddy simulation in an unstructured mesh environment, Ph.D. thesis, Stanford University (2014).

[60] K. Suga, T. Sakamoto, Y. Kuwata, Algebraic non-equilibrium wall-stress modeling for large eddy simulation based on analytical integration of the thin boundary-layer equation, Phys. Fluids 31 (7) (2019) 075109.